Acta Acustica 2025, **9**, 18

https://doi.org/10.1051/aacus/2025007

Available online at:
https://acta-acustica.edpsciences.org

SCIENTIFIC ARTICLE OPEN ACCESS

Investigation and optimal design of band gap tunability in fractal phononic crystals

Shuai Yang[1,2], Jia-Hao Yin[3], Xiao-Jing Zhu[1,2], Kai Wang[4,*], Shi-ke Zhang[1,2], Lu Cao[4], Peng-Yu Guo[4], and Yong Liu[4]

[1]School of Civil Engineering and Architecture, Anyang Normal University, Anyang 455000, China
[2]Henan Province Engineering Technology Research Center for Digital Intelligent Building and Low Carbon Building Materials, Anyang Normal University, Anyang 455000, Henan, China
[3]School of Civil and Environmental Engineering, The University of New South Wales, Sydney 2052, Australia
[4]National Innovation Institute of Defense Technology, Academy of Military Science, Beijing 100071, China

Received 4 November 2024, Accepted 5 February 2025

Abstract – This study investigates the properties of band gaps of circular core filling fractal phononic crystals (CCFFPCs), specifically focusing on the impact of different filling positions on the frequency of band gaps. The research demonstrates that core filling at the central positions significantly influences the formation and widening of low-frequency band gaps, while filling at corner edges predominantly affects mid-frequency band gaps, and filling at edge centers effectively opens and broadens high-frequency band gaps. These results reveal the relationship between filling positions and band gap tuning, providing a theoretical foundation for precise band gap control across a full frequency range. Moreover, this study is the first to systematically clarify the impact of core filling positions on band gap frequencies, expanding the design strategies for band gaps in fractal phononic crystals. Furthermore, this study employs genetic algorithm optimization to achieve the maximum band gap width at different frequencies, enhancing the practical value of fractal phononic crystals in engineering applications. This research deepens theoretical understanding and provides valuable guidance for optimizing their use in broadband acoustic control and energy harvesting applications.
Keywords: Fractal phononic crystal, Band gap tunability, Genetic algorithm, Optimal design

1 Introduction

Phononic crystals are a novel type of artificial structure composed of different materials and geometric configurations arranged periodically. In recent years, the propagation characteristics of waves in phononic crystals have garnered widespread attention. The most notable characteristic of phononic crystals is the presence of band gaps, which can be attributed primarily to the principles of Bragg scattering [1] and local resonance [2]. This property significantly enhances the applications of phononic crystals, including filters [3–5], waveguides [6–11], noise reduction [12,13], energy harvesting [14–16] and acoustic sensors [17–20], among others.

Since 1990, inspired by photonic crystals, research on phononic crystals has garnered significant attention from researchers and has rapidly developed. The current research on phononic crystals can mainly be divided into three aspects: the study and verification of phononic crystal theories [21,22], the design and fabrication of phononic crystal with wave control capabilities [23–26], and the multidisciplinary integration of phononic crystals [27–29]. Among these studies, fractal phononic crystals, as an exploration of basic phononic crystal structures, have attracted widespread attention due to their multiple band gaps, self-similarity, and the ability to generate band gaps at lower frequencies.

Kuo et al. [30] designed a microscale fractal-like phononic band gap structure made from aluminum nitride (AlN) that achieves high-frequency band gaps. Liu et al. [31] introduced a two-dimensional phononic crystal model based on a T-square fractal design, examining the differences in band structures between fractal and non-fractal phononic crystals with identical filling ratios. They concluded that fractal designs significantly influence the band structure of two-dimensional phononic crystals. Wang et al. [32] investigated the band gap in Sierpinski triangle fractal porous phononic crystals (FPPCs) and assessed the impact of fractal hierarchy on the band gap. Huang et al. [33] explored the multiple band gap

*Corresponding author: cxywangkai@163.com

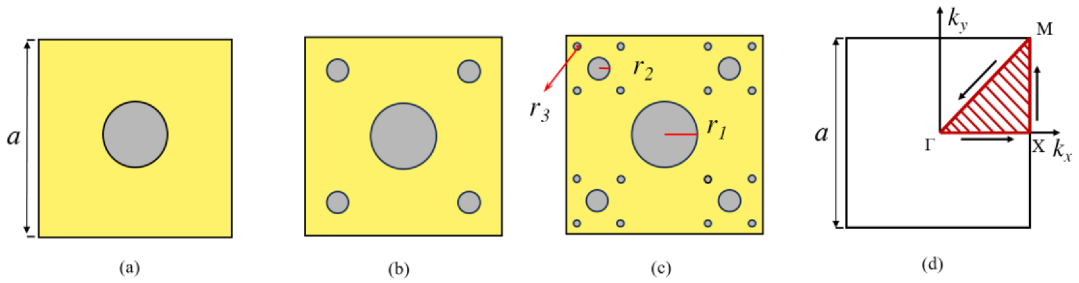

Figure 1. CCFFPCs unit cells at different stage for $K = 1$ and $M = 3$: (a) $L = 1$, (b) $L = 2$, (c) $L = 3$, (d) Brillouin zone.

properties of quasi-Sierpinski fractal phononic crystals, demonstrating that fractal phononic crystals enhance the formation of multiple wider band gaps, especially in second-stage case. Reviewing the existing research on fractal PCs, we find that most studies primarily focus on exploring the advantages of fractal PCs compared to basic PCs. However, research on the influence of the position and filling ratio of internal fillers within fractal PCs on their band structure is relatively scarce.

In this study, we propose a novel CCFFPCs, which can significantly influence the opening and widening of low, medium, and high-frequency band gaps by strategically placing cores at different locations within the unit cell, compared to traditional fractal phononic crystals. Building on these findings, a set of guidelines for facilitating the opening of these band gaps in CCFFPCs was proposed. Additionally, this study employs genetic algorithm optimization to design multiple CCFFPCs with maximum band gap widths at different frequencies, not only validating the accuracy of the proposed theory but also enhancing the engineering application value of fractal phononic crystals.

2 Mathematical formulation

2.1 Calculation of unit cells with CCFFPCs

In exploring the physical characterization of phononic crystals, unit cell is typically chosen to describe the periodic structure and physical properties of the overall crystal. According to Bloch's theorem [34], the wave function of a crystal can always be expressed as the product of a periodic function and a plane wave. Therefore, we initiated our study by analyzing unit cell with CCFFPCs.

The elastic waves, propagating in the transverse plane, can be separated into the mixed anti-plane shear mode and the in-plane mode, indicating that the displacement vectors are not influenced by the z-coordinate. Therefore, only the in-plane mode is considered in this study. Figure 1 shows the two-dimensional CCFPCs considered in this paper, illustrating the unit cells of CCFFPCs at different stages. Figures 1a–1c correspond to the first-stage, second-stage, and third- stage CCFFPCs, respectively, while Figure 1d shows the irreducible Brillouin zone of a square unit cell. In these structures, the yellow regions represent epoxy resin, and the gray regions represent steel. The material parameters are detailed in Table 1.

Table 1. The material parameters of CCFFPCs.

Material	ρ(kg/m^3)	E (Pa)	v
Epoxy resin	1180	4.35e9	0.36
Steel	7780	2.11e11	0.3

The design principle of these CCFFPCs begins with a complete phononic crystal structure with a square unit cell of size length $a = 1.2$ m, which is divided equally into nine smaller squares. A circular steel core is then inserted in the center to form the first-stage CCFFPCs. On this basis, the same procedure is repeated in the four corner regions to establish the second-stage CCFFPCs. This iterative process continues for L iterations, ultimately resulting in an L-stage CCFFPCs unit cell. During the generation of the CCFFPCs, the center of the unit cell is set as the origin of coordinates. At the L-stage, the number of grids in the structure is $N = M^{2L}$, where M represents the number of grids in the x or y direction of the first-stage CCFFPCs unit cell. K refers to the number of gray squares in the x or y direction of the first-stage CCFFPCs. For example, as shown in Figure 1a, when $L = 1$, $K = 1$, $M = 3$, the square unit cell is divided into 3 equal parts in both the x and y directions, with each part occupying one portion in the respective directions. Meanwhile, we define the radius of the central circle as r_1, the radius of the circular cores located at the edge corner positions as r_2, and the radius of the four corner circles as r_3.

In this paper, the finite element method is used to calculate the band structure of the proposed structures. According to Bloch's theorem, for two-dimensional phononic crystals, the displacement ($\mathbf{U}(\mathbf{r})$) on the boundary of the unit cell satisfies:

$$\left[\mathbf{\Omega}(\mathbf{k}) - \omega^2\mathbf{M}\right] \cdot \mathbf{U} = 0 \tag{1}$$

where $\mathbf{a}$ is the lattice constant, and $\mathbf{r}$ is the position vector in space. The discrete form of the characteristic equation within the unit cell can be written as:

$$\left(\mathbf{K} - \omega^2\mathbf{M}\right)\mathbf{U} = 0. \tag{2}$$

In the equation, $\mathbf{K}$ is the stiffness matrix of the unit cell, and $\mathbf{M}$ is the mass matrix of the unit cell. By combining

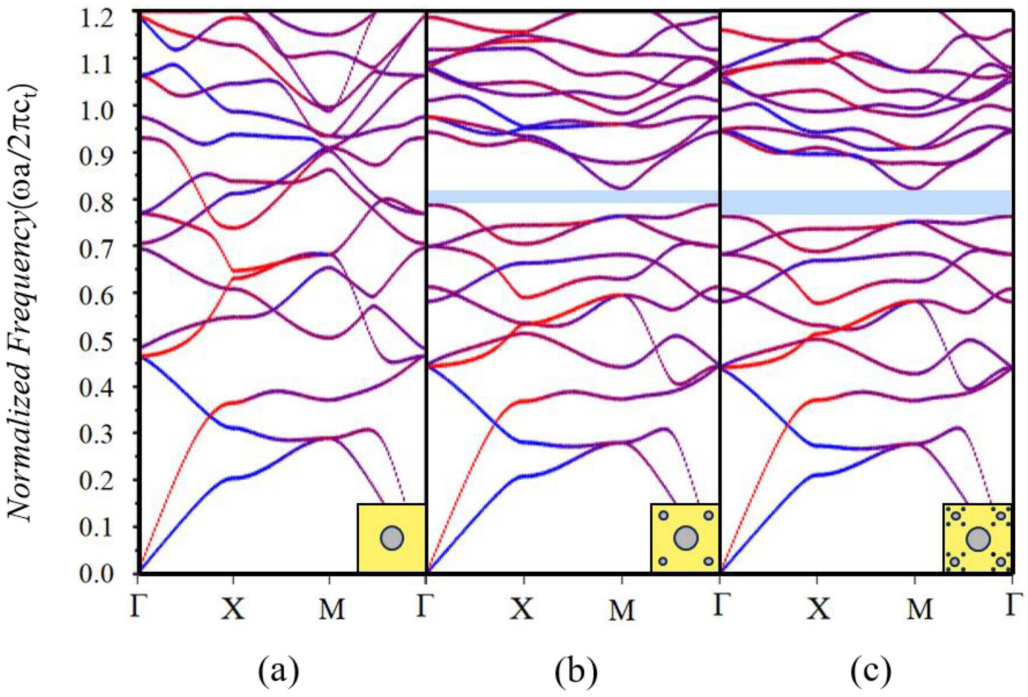

Figure 2. Band structure of the CCFPC at $K = 1$, $M = 3$: (a) first-stage structure, (b) second-stage structure, (c) third-stage structure.

the displacement equation at the boundary of the unit cell, i.e., equation (1), the characteristic equation of the unit cell can be directly solved using the finite element software COMSOL Multiphysics. The obtained eigenvalues can be used to plot the band structure of the unit cell.

3 Results and discussion

3.1 Analysis of band structure for CCFFPCs at different stages and filling ratios

To investigate the band gaps of CCFPC under different stages and filling ratios (f), we calculated the band structures of CCFFPCs with stages ranging from first to third. The specific f is $K = 1$, $M = 3$; $K = 2$, $M = 4$; $K = 3$, $M = 5$; and $K = 4$, $M = 6$. The frequency of band structures is normalized by $\Omega = \omega * a/(2\pi c_t)$, where $c_t = (G/\rho)1/2$ is the shear wave speed and G is the shear modulus of the matrix. In the band structures, the color of the points represents the polarization in the direction of wave propagation, defined as:

$$m_p = \frac{\int_A |u_L|^2 \, \mathrm{d}A}{\int_A \left(|u_L|^2 + |u_S|^2\right) \mathrm{d}A}. \tag{3}$$

The displacement components, u_L and u_S, refer to the directions parallel and perpendicular to the wave vector, respectively. The integration is performed over the entire unit cell. Equation (3) shows that the polarization of a specific wave evolves from $m_p = l$ (characterizing a pure longitudinal mode, presented by red) to $m_p = 0$ (characterizing a pure transverse mode, presented by blue).

Figure 2 presents the band structures for the CCFPC from first to third stage at $K = 1$, $M = 3$. In Figure 2a, it is noted that there is no band gap at the first stage. Conversely, Figure 2b reveals that as the stage of the CCFFPCs increases, the low-frequency bands become increasingly compressed. Notably, a full band gap emerges between the 10th–11th bands within the frequency range of $\Omega = 0.786$ to 0.822. Figure 2c further demonstrates that at the third stage, the 10th–11th band gap widens due to further compression of the bands. Overall, under the condition of $K = 1$, $M = 3$, a 10th–11th band gap opens and its width increases with the stage increases.

It is worth noting that by observing the color changes of different bands in the $\Gamma - X$ direction, as illustrated Figure 2. This reveals that the 1st band corresponds to the transverse mode, the 2nd band rapidly transitions from the longitudinal mode to the transverse mode, the 3rd band also rapidly transitions from the transverse mode to the longitudinal mode, the 4th band corresponds to the transverse mode, while the other bands are all mixed modes.

Figure 3 displays the band structures of the CCFPC at $K = 2$, $M = 4$ for different stages. Compared to Figure 2, the band gaps in Figure 3 are more pronounced due to the increased f. In Figure 3a, a relatively wide low-frequency full band gap appears between the 3rd–4th bands at $\Omega = 0.387$–0.513. As the stage of the CCFFPCs increases, the low-frequency band gaps gradually decrease in width. In the second stage band structure of Figure 3b,

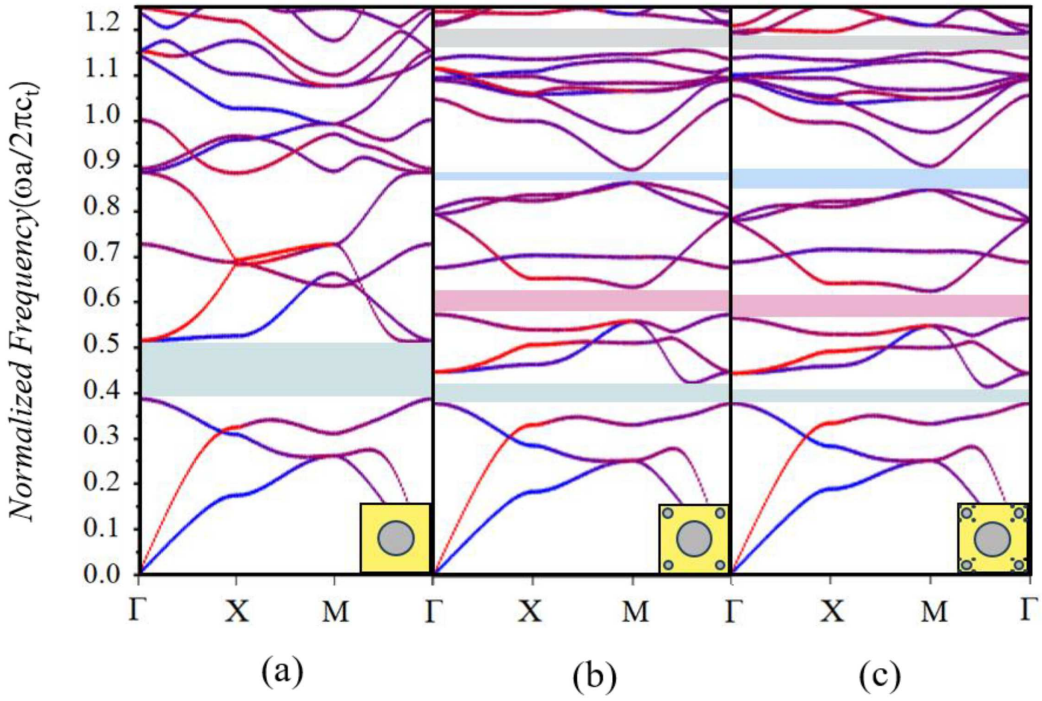

Figure 3. Band structure of the CCFPC at $K = 2$, $M = 4$: (a) first-stage structure, (b) second-stage structure, (c) third-stage structure.

the full band gaps can be observed at $\Omega = 0.351$–0.458, $\Omega = 0.612$–0.733, and $\Omega = 1.172$–1.201. When the stage increases to $L = 3$, the 3rd–4th band gaps and the 6th–7th band gaps further decrease, while the 10th–11th band gap slightly widens. This further demonstrates that as the stage of the CCFPC increases, the width of the low-frequency band gaps decreases, while the high-frequency band gaps increases.

In Figure 4, the f of the CCFPC increases further, with K and M raised to 3 and 5, respectively. As depicted in Figure 4a, a broad full band gap appears between the 3rd–4th bands at $\Omega = 0.342$–0.654. With the further increase of L, in Figures 4b and 4c, the 3rd–4th band gap gradually decreases, while a wider band gap emerges between the 6th–7th bands. This band gap appears at $\Omega = 0.612$–0.733 in the second-stage structure and at $\Omega = 0.603$–0.724 in the third-stage structure. Moreover, a relatively narrow full band gap can be observed in the 13th–14th bands, located at $\Omega = 1.172$–1.201 and $\Omega = 1.176$–1.201, respectively. By comparing the band structures of the first-stage to third-stage CCFFPCs under different f in Figures 2–4, it is evident that the width of the band gaps in the mid to low frequency significantly widens as the f increases. Additionally, with the increase in f of the CCFFPCs, the entire band structure is notably stretched and flattened. Concurrently, the emergence of a low-frequency band gap results in the compression of the bands at lower frequencies. Notably, as illustrated in Figure 2a, the 3rd band initially exhibits a transverse wave mode, while the 4th band is characterized as a longitudinal wave mode. As the 3rd–4th band gap opens, the 3rd band mode transitions into a mixed mode, whereas the 4th band mode evolves into a transverse wave mode.

Figure 5 illustrates the first-stage to third-stage band structure of the CCFPC under the condition of $K = 4$, $M = 6$. As the f increases, compared to the full band gap that appears between the 3rd–4th bands in Figure 4a, the band gap of the first-stage CCFPC under this condition is wider. Furthermore, an increase in the L leads to the compression of low-frequency band gap, while concurrently opening mid and high-frequency band gaps. This results in the emergence of three distinct and wider full band gaps, which are observed between the 5th–6th band, the 6th–7th band, and the 13th–14th band. At $L = 2$, full band gaps appear at $\Omega = 0.340$–0.497, $\Omega = 0.579$–0.644, $\Omega = 0.665$–0.843, and $\Omega = 1.249$–1.356, while at $L = 3$, the full band gaps appear at $\Omega = 0.340$–0.489, $\Omega = 0.571$–0.635, $\Omega = 0.657$–0.836, and $\Omega = 1.254$–1.357. A comparison of the full band gap distributions between 2nd–3rd reveals a narrowing of the band gaps in the mid and low-frequency ranges with increasing stage, while the high-frequency band gaps exhibit a widening trend.

This section delves into the distribution of band gaps of the CCFPC under different stages and f. By comparing the aforementioned figures, it can be observed that as the f increases, the width of the band gaps becomes wider. Additionally, as the stage of the structure increases, the low-frequency band gaps are compressed, and new band gaps emerge between the mid to high-frequency bands. In summary, the f of the CCFFPCs affects the width of band gaps, while the stage of the structure affects both the specific frequencies at which band gaps occur and the number of emerging band gaps.

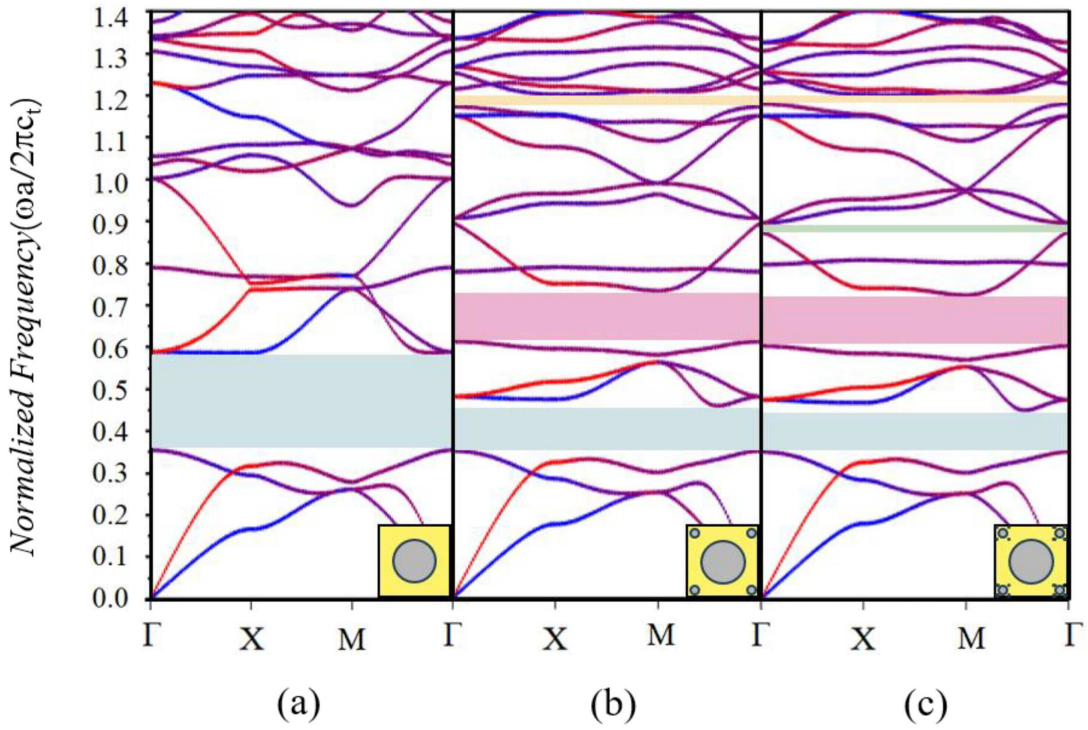

Figure 4. Band structure of the CCFPC at $K = 3$, $M = 5$: (a) first-stage structure, (b) second-stage structure, (c) third-stage structure.

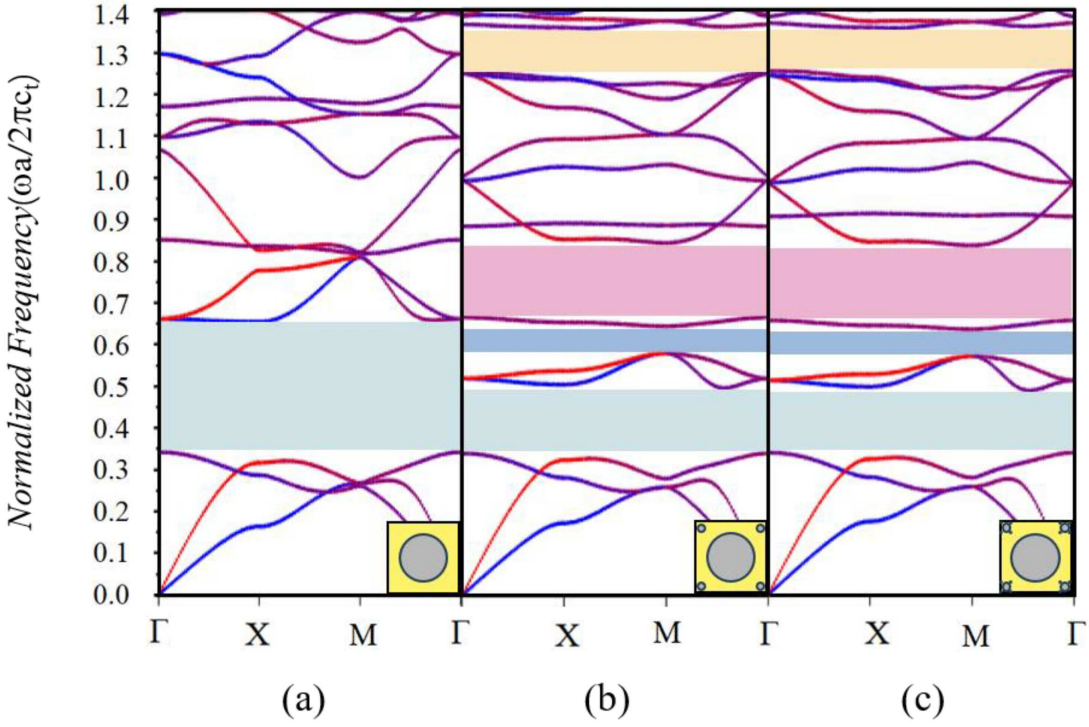

Figure 5. Band structure of the CCFPC at $K = 4$, $M = 6$: (a) first-stage structure, (b) second-stage structure, (c) third-stage structure.

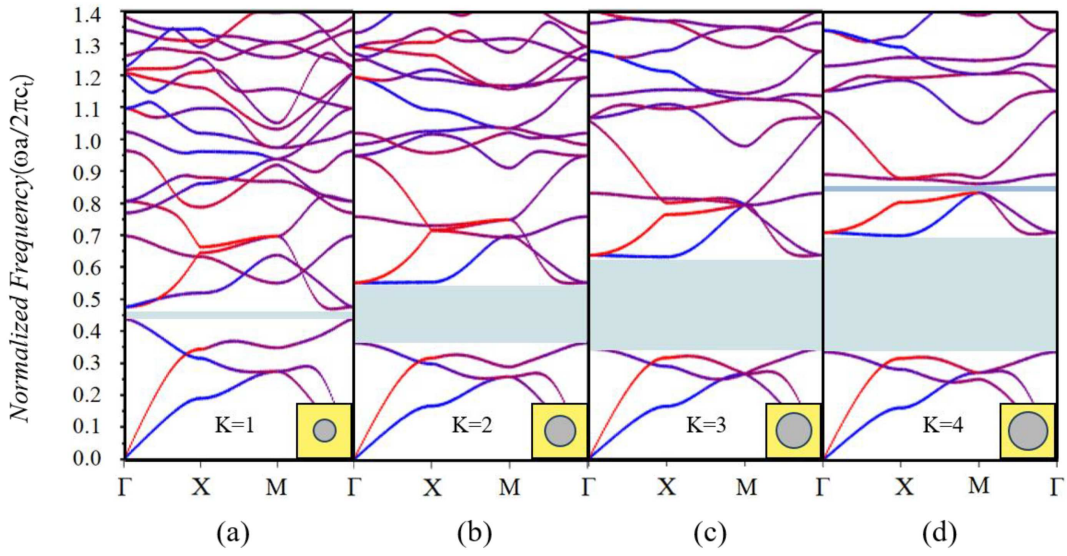

Figure 6. Band structure of the second-stage CCFFPCs with a circular core under different filling conditions after equivalent area treatment: (a) $K = 1$, $M = 3$, (b) $K = 2$, $M = 4$, (c) $K = 3$, $M = 5$, (d) $K = 4$, $M = 6$.

3.2 Comparison between CCFFPCs and equivalent area PC

In the previous section, we conducted a detailed discussion on the influence of the three parameters K, M, and L on the distribution and width of the full band gaps of the CCFPC. In this section, we apply an equivalent area treatment to the CCFFPCs by defining the total area of the core in the CCFFPC under different L, K, and M filling conditions as the area of the core in the basic phononic crystal. This approach helps further investigate the relationship between the band gaps of the basic phononic crystals with a circular core and the core filling fraction.

As shown in Figure 6, Figures 6a–6d represent the band structure of the basic phononic crystal under equivalent area for the second-stage CCFFPCs when $K = 1$ to $K = 4$, respectively. It can be clearly observed that, as f varies from $K = 1$ to $K = 3$, full band gaps all occur between the 3rd–4th bands, respectively at $\Omega = 0.437$–0.469, $\Omega = 0.366$–0.552, and $\Omega = 0.345$–0.631. However, when f is $K = 4$, $M = 6$, the 3rd–4th band gap further widens, and a new, narrower full band gap with a width of 0.035 appears between 5th–6th bands. Comparing the band gap distribution of the basic phononic crystal under different f, it is found that after equivalent area treatment, as the f of the central core increases, the width of the low-frequency band gap gradually increases. Based on this phenomenon, we can infer that in CCFFPCs, the core located in the middle plays a direct role in the formation of its low-frequency band gaps.

Figure 7 illustrates the band structure of the basic phononic crystal after equivalent area treatment for the third-stage CCFPC under different f. In Figure 7a, for the structure under $K = 1$ and $M = 3$, the band gap distribution is observed between $\Omega = 0.422$–0.479 with a width of 0.057. In contrast, the full band gap in Figure 7b occurs between $\Omega = 0.362$–0.563 with a width of 0.201. Figure 7c shows the band gap distribution between $\Omega = 0.344$–0.639 with a width of 0.295 under $K = 3$, $M = 5$ conditions. In Figure 7d, the full band gaps appear between $\Omega = 0.338$–0.706 and $\Omega = 0.833$–0.868. Combining the conclusions drawn from Figure 6, these results further confirm that the f of the central core in the CCFPC significantly influences the distribution of low-frequency band gaps. However, it is important to note that regardless of the f of the central circular core, a band gap never appears at higher frequency. Therefore, through a comparison of the band gaps presented in Section 3.1, we deduce that the cores located at the edges of the CCFFPCs have a certain impact on the opening of band gaps in the mid to high frequency bands.

3.3 The impact of different positions filling cores within the basic phononic crystal on its band structure

To investigate the relationship between core positions in phononic crystals and positions of band gap formation, we analyzed the impact of varying f under different edge filling conditions on band gap opening.

First, based on a second-stage CCFFPCs with a f condition of $K = 2$, $L = 2$, building a basic phononic crystal with r_1 at $0.1667\,a$ and r_2 at 0 m, $0.0417\,a$, $0.0833\,a$, $0.125\,a$, and $0.1625\,a$, respectively. The band structures of these configurations were calculated, as shown in Figure 8a–8e. It is evident that as r_2 increases, the band gap transitions from nonexistent to present and gradually widens. Notably, when r_2 reaches 0.1 m, full band gaps first appear at $\Omega = 0.697$–0.754, $\Omega = 0.828$–0.849, and $\Omega = 0.984$–0.996, located between the 10th–11th bands, 11th–12th bands, and 15th–16th bands, respectively. As r_2 further increases to $0.125\,a$, the width of the 10th–11th band gap decreases to 0.046, the 11th–12th band

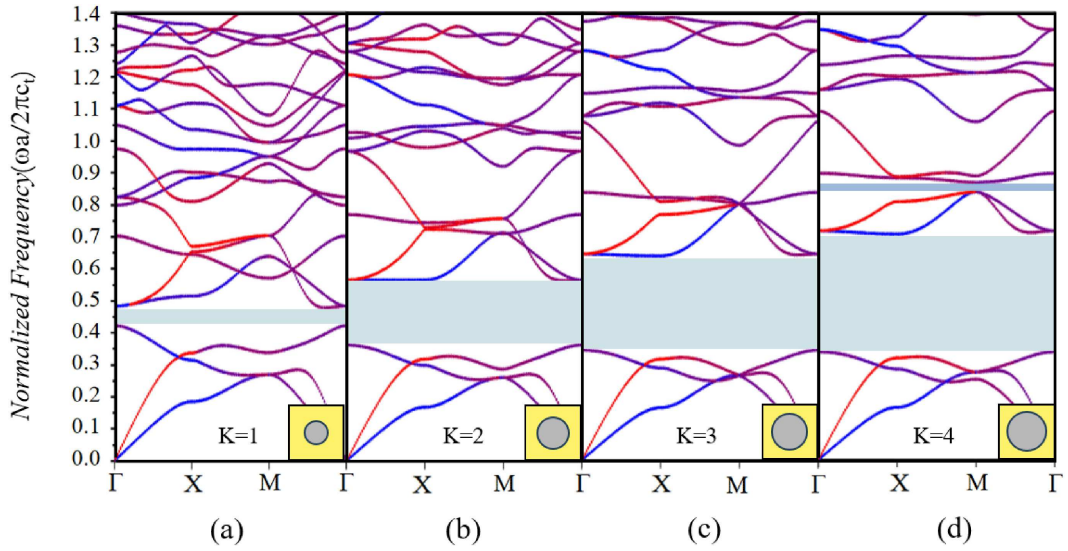

Figure 7. Band structure of the third-stage CCFFPCs with a circular core under different filling conditions after equivalent area treatment: (a) $K = 1$, $M = 3$, (b) $K = 2$, $M = 4$, (c) $K = 3$, $M = 5$, (d) $K = 4$, $M = 6$.

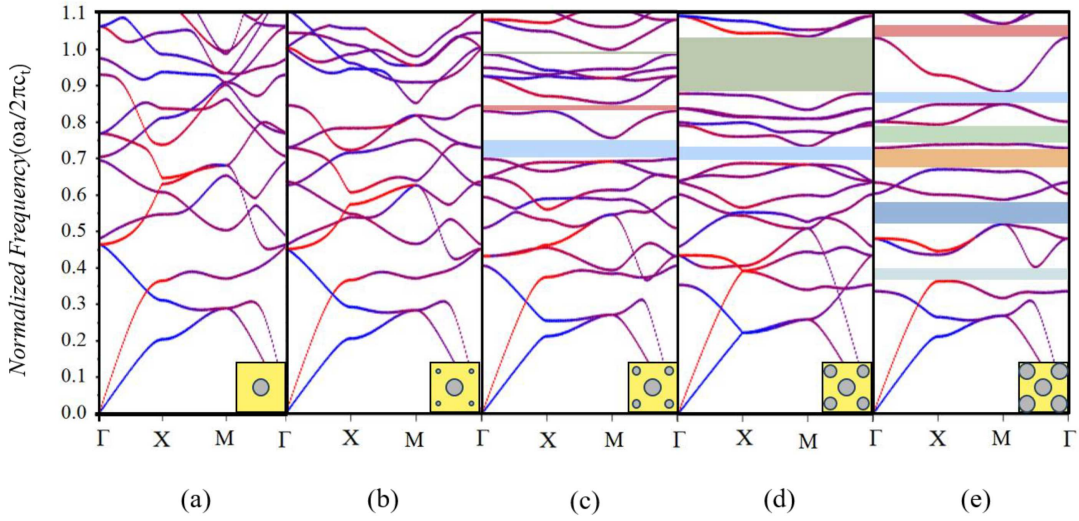

Figure 8. Based on the CCFFPCs with a filling ratio of $K = 2$ and $M = 4$, keeping the radius of the central circular core $r_1 = 0.1667\,a$ constant, and filling circular cores with different radii into the corner edges of its basic phononic crystal, the band structures of the structures are as follows: (a) $r_2 = 0\,\mathrm{m}$, (b) $r_2 = 0.0417\,a$, (c) $r_2 = 0.0833\,a$, (d) $r_2 = 0.125\,a$, (e) $r_2 = 0.1625\,a$.

gap completely disappears, while the 15th–16th band gap significantly widens, reaching a width of 0.156. It is noteworthy that in Figure 8e, several new full band gaps are observed to open between the bands in the mid-frequency, accompanied by a further compression of the lower-order bands.

Comparing the results presented in Figure 8, it is observed that when $r_2 = 0.0833\,a$, the band gap that appears is not particularly obvious due to the low f. Therefore, based on a second-stage CCFFPCs with a f of $K = 3$ and $M = 5$, we maintained the r_1 at $0.3\,a$ and adjusted the r_2 to calculate its band structure, as shown in Figure 9. As a result of the increased f, a markedly wide full band gap emerges between the 3rd–4th bands of the basic phononic crystal, as illustrated in Figure 9a.

As r_2 increases, particularly at $0.05\,a$, we observe the emergence of band gaps at higher frequency positions. Specifically, full band gaps are noted at $\Omega = 0.352$–0.487, $\Omega = 0.598$–0.615, $\Omega = 0.647$–0.727, $\Omega = 1.177$–1.212, and $\Omega = 1.321$–1.344. As r_2 continues to increase, the low-frequency band gap gradually decreases, while the 6th–7th band gap significantly widens, increasing from the original 0.08 to 0.178 and then to 0.454. Notably, in Figure 9e, the 8th–9th band gap is opened, which is probable because the 9th band is a flat band. The mode shapes at the frequency corresponding to this band, indicated by the arrows in Figure 9, demonstrate that stress is predominantly concentrated on the cores filled in at the corner edges. This suggests that embedding cores in the corner edge regions directly influences the opening of this

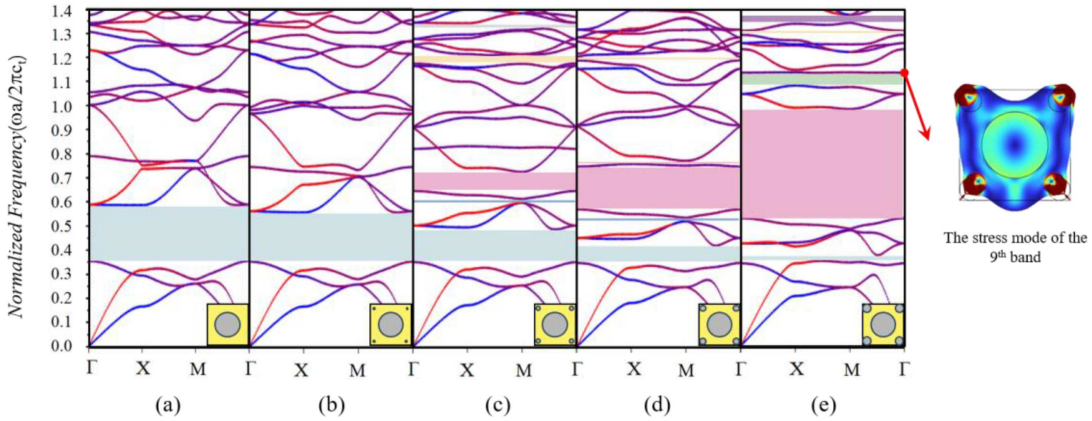

Figure 9. Based on the CCFFPCs with a filling ratio of $K = 3$ and $M = 5$, keeping the radius of the central circular core $r_1 = 0.3\,a$ constant, and filling circular cores with different radii into the corner edges of its basic phononic crystal, the band structures of the structures are as follows: (a) $r_2 = 0\,\mathrm{m}$, (b) $r_2 = 0.025\,a$, (c) $r_2 = 0.05\,a$, (d)$r_2 = 0.075\,a$, (e) $r_2 = 0.0992\,a$.

band gap. By integrating the result from Figures 7 and 8, it becomes apparent that filling the cores in the edge corners of the basic phononic crystal substantially facilitates the opening of band gaps within the mid to high frequency, with a particularly significant impact on the width of band gaps at mid frequency.

Figures 8 and 9 demonstrate the effects of filling circular cores into the edge corners of the basic phononic crystal on the band gap, considering various central core radii. To further investigate whether filling cores at any position along the edges of the basic phononic crystal can achieve the aforementioned effects on the band gaps, we maintained $r_1 = 0.3\,a$ and moved the cores from the corner positions to the central edge positions for filling. The band structures corresponding to these different configurations were computed, and the results are presented in Figure 10.

In comparison to Figure 9, the placement of cores in the central edge positions of the basic phononic crystal resulted in the emergence of a relatively narrow high-frequency band gap when $r_2 = 0.025\,a$, excluding the band gap between the 3rd–4th low-frequency bands. As r_2 increases, 16th–17th band gap gradually widens, with its width expanding from 0.021 to 0.038 and then to 0.097. Additionally, when $r_2 = 0.0992\,a$, a new wide band gap with a width of 0.053 appears between 8th–9th bands. An analysis of the results presented in Figure 10 reveals that filling cores in the central edge positions has a more pronounced effect on the formation and widening of high-order band gaps compared to filling cores in the edge corner positions. Conversely, the impact on the band gaps at mid frequency is comparatively smaller. This finding indicates the significant influence of both the filling position and core size on the band gaps. Notably, while filling at the central edge positions markedly affects the formation and adjustment of high-frequency band gaps, the edge corner positions play a more critical role in the formation and modulation of mid-frequency band gaps.

Building upon the aforementioned research, we extended our investigation to a third-stage CCFFPCs under the f conditions of $K = 3$ and $M = 5$, exploring the impact of filling smaller cores with r_3 at the four corners on the band structure. Figures 11a–11d respectively show the band structures when $r_1 = 0.1667\,a$, $r_2 = 0.06\,a$, and r_3 is 0 m, $0.0479\,a$, $0.0958\,a$, and $0.1917\,a$. The increase in r_3 has a minimal influence on the overall f, resulting in negligible alterations to the band structure. However, it is noteworthy that as the radius increases, the widths of the band gaps at both low and high frequency decrease, while the width of the mid-frequency band gap increases. Furthermore, in Figure 11e, we observe a new band gap opening between the 8th–9th bands. This phenomenon further verifies that filling cores at the edge corner positions within the basic phononic crystal facilitates the opening and widening of band gaps in the mid-frequency.

In summary, for a basic phononic crystal, filling a core at the central position greatly influences the formation of low-frequency band gaps. Conversely, filling cores at the edge corners has a more significant effect on the mid-frequency band gaps. Furthermore, filling cores at the central positions of the edges can effectively open and widen the high-frequency band gaps. Consequently, the filling of cores of different sizes and positions significantly modulates the band gaps at various frequencies, providing theoretical guidance for the design of phononic crystals.

3.4 Inverse design of quasi-fractal PC using genetic algorithms

The findings presented in the previous section indicate that by varying the f and positions of the cores, it is possible to control both the generation and the width of band gaps across various frequencies.

Genetic algorithm (Genetic Algorithm, GA) was first proposed by Professor Holland and his students of the University of Michigan in the late 1960s and early 1970s. It is an efficient, parallel global search method that draws inspiration from Darwin's theory of evolution and

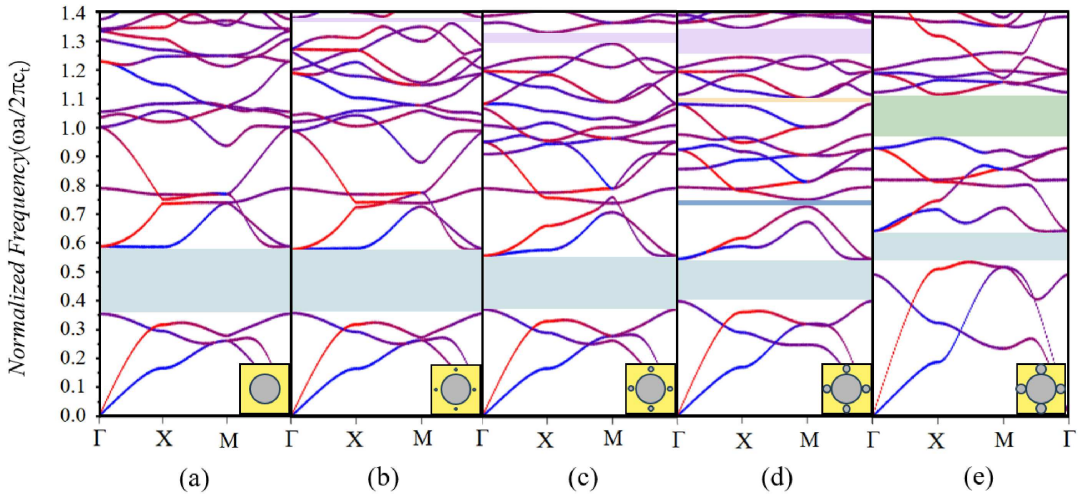

Figure 10. Based on a second-stage CCFFPCs with a filling ratio of $K = 3$ and $M = 5$, keeping the central circular core radius $r_1 = 0.3\,a$ constant, different radii of circular cores are filled into the central edge positions of its basic phononic crystal. The band structures of the configurations are as follows: (a) $r_2 = 0\,\mathrm{m}$, (b) $r_2 = 0.025\,a$, (c) $r_2 = 0.05\,a$, (d)$r_2 = 0.075\,a$, (e) $r_2 = 0.0992\,a$.

Mendel's theory of genetics [35,36]. It is an optimization method that automatically acquires and accumulates knowledge about the search space during the search process and adaptively controls the search process. In this section, we employed GA based on COMSOL with MATLAB to obtain structural configurations with the widest low-frequency band gap, mid-frequency band gap, and the maximum total band gap, respectively, the flow chart is shown in Figure 12.

The optimization problem for the inverse design of quasi-fractal PC can be described as

$$\sum \max \Psi_{i-i+1}(r_1, r_2, r_3) = \sum (\min Fre_{i+1} - \max Fre_i). \quad (4)$$

(low-frequency: $i = 3$, mid-frequency: $i = 6$, overall: $i = 1{\sim}10$)

$$\text{s.t.} \begin{Bmatrix} 2r_1 + 4r_2 + 8r_3 \le a \\ 0 < r_1 \le a/2 \\ 0 < r_2 \le a/4 \\ 0 < r_3 \le a/8 \end{Bmatrix}. \quad (5)$$

Here, Ψ denotes the desired band gap width, which is a function of r_1, r_2 and r_3. min Fre_{i+1} represents the minimum of the $i+1$ band, while max Fre_i denotes the maximum of the i band. The condition for optimization with the widest low-frequency band gap is defined by setting $i = 3$, while the condition for the widest mid-frequency band gap is defined by setting $i = 6$. The desired structural configuration can be obtained by using genetic algorithms for optimization.

As shown in Figure 13, Figure 13a illustrates the band structure under the condition where the 3rd–4th band gap is the widest within a second-stage fractal PC. At this condition, the structural parameters are $r_1 = 0.4582\,a$ and $r_2 = 0.0083\,a$, and the width of the 3rd–4th band gap is 0.635. It is evident that a sufficiently large r_1 results in the widest 3rd–4th band gap. This optimized outcome further verifies the theory that the central core primarily influences the opening and widening of low-frequency band gaps. Figure 13b shows the 6th–7th band gap is the widest, with the geometric parameters of the structure being $r_1 = 0.3154\,a$ and $r_2 = 0.0885\,a$, and the width of the band gap being 0.412. This optimized result also supports the theory that filling cores at the edge corners primarily affects the width of mid-frequency band gaps. In Figure 13c, the band structure under the condition where the total width of the band gaps is the widest in a second-stage fractal PC is presented, with the geometric parameters of the structure being $r_1 = 0.4604\,a$ and $r_2 = 0.0083\,a$. This calculation reveals that low-frequency band gaps are more easily opened compared to high-frequency band gaps.

Figure 14 illustrates the comparison between the band structure and the response spectrum along the $\Gamma{-}X$ direction of the second-stage fractal PC when the 3rd–4th band gap is the widest. It is clearly observed that the transmission rate in the response spectrum is extremely low within the frequency range of the 3rd–4th bands, which corresponds to the wide band gap between these bands in the band structure. Additionally, other band gaps observed in the band structure also align with the corresponding regions in the response spectrum, further confirming the accuracy of the optimization methods and computational results presented in this study.

Similarly, the band structure of the third-stage fractal PC optimized by the genetic algorithm is shown in Figure 15. Figure 15a depicts the band structure corresponds to the widest 3rd–4th band gap, with the geometric parameters being $r_1 = 0.4417\,a$, $r_2 = 0.0083\,a$, and $r_3 = 0.0083\,a$. As theorized above, to achieve the widest low-frequency band gap, the size of the central circular core within the structure needs to be maximized.

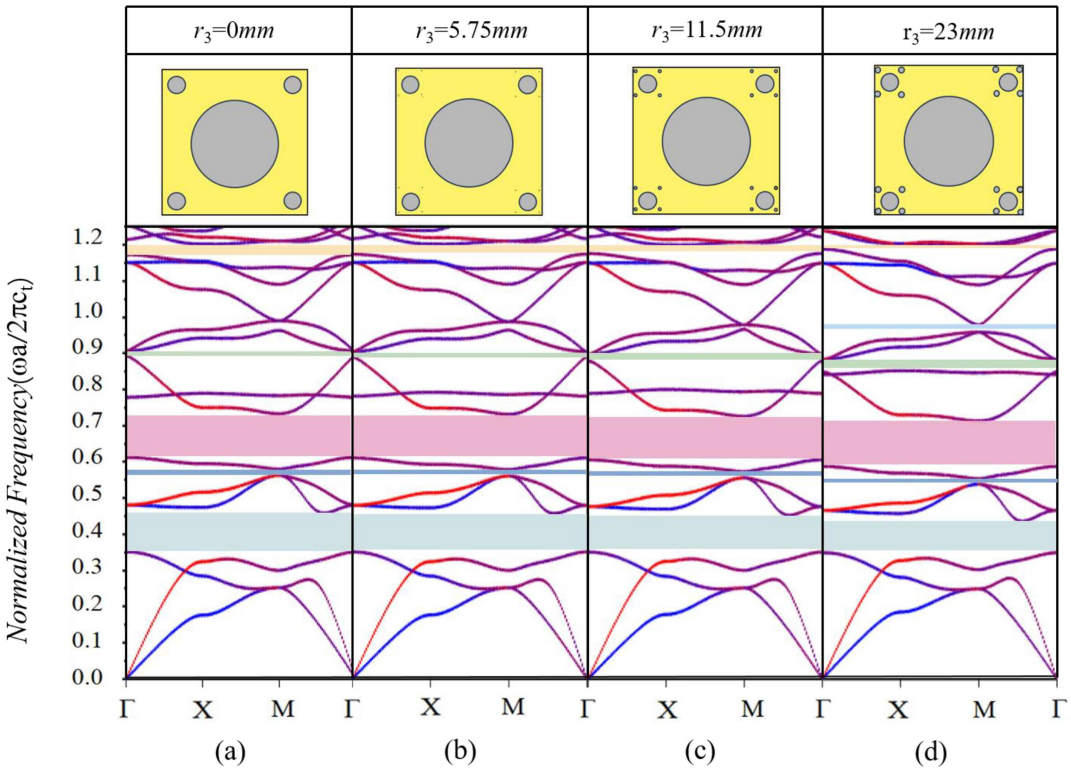

Figure 11. Based on a third-stage CCFFPCs with a filling ratio of $K = 3$ and $M = 5$, while maintaining $r_1 = 0.1667\,a$ and $r_2 = 0.06\,a$ unchanged, circular cores of different radii are filled at the center of the edge of the basic phononic crystal. The band structures of the configurations are as follows: (a) $r_3 = 0\,\mathrm{m}$, (b) $r_3 = 0.0479\,a$, (c) $r_3 = 0.0958\,a$, (d) $r_3 = 0.1917\,a$.

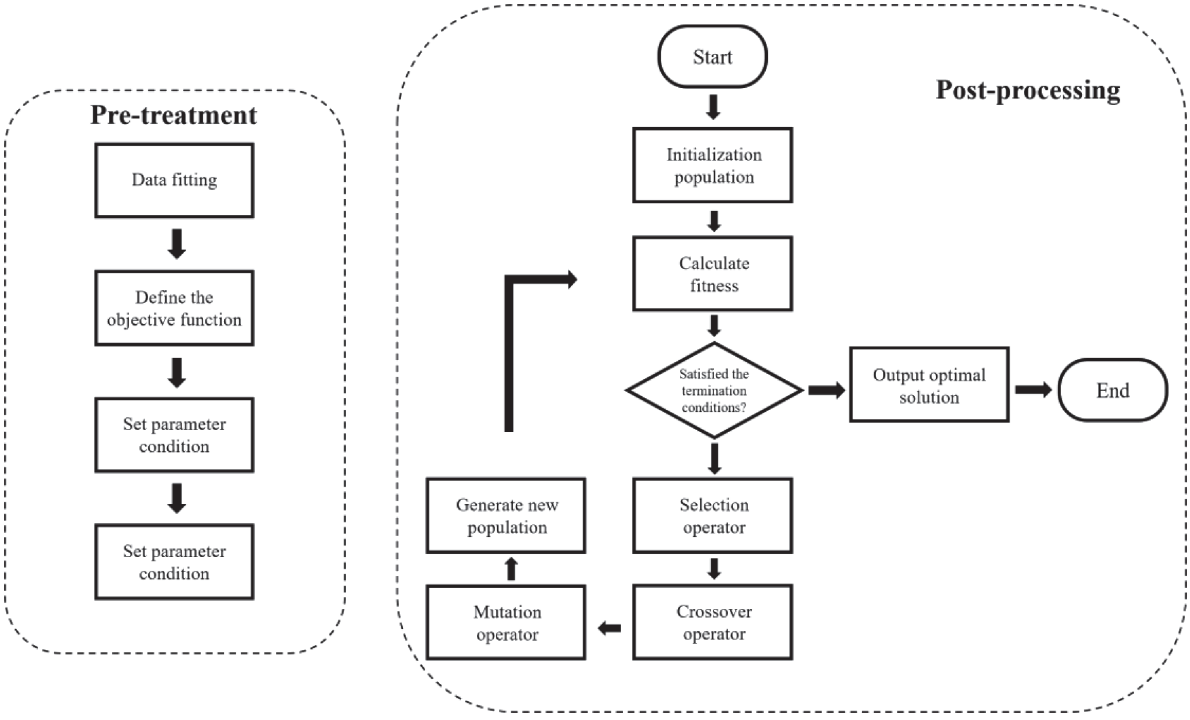

Figure 12. Structural optimization calculation flow chart.

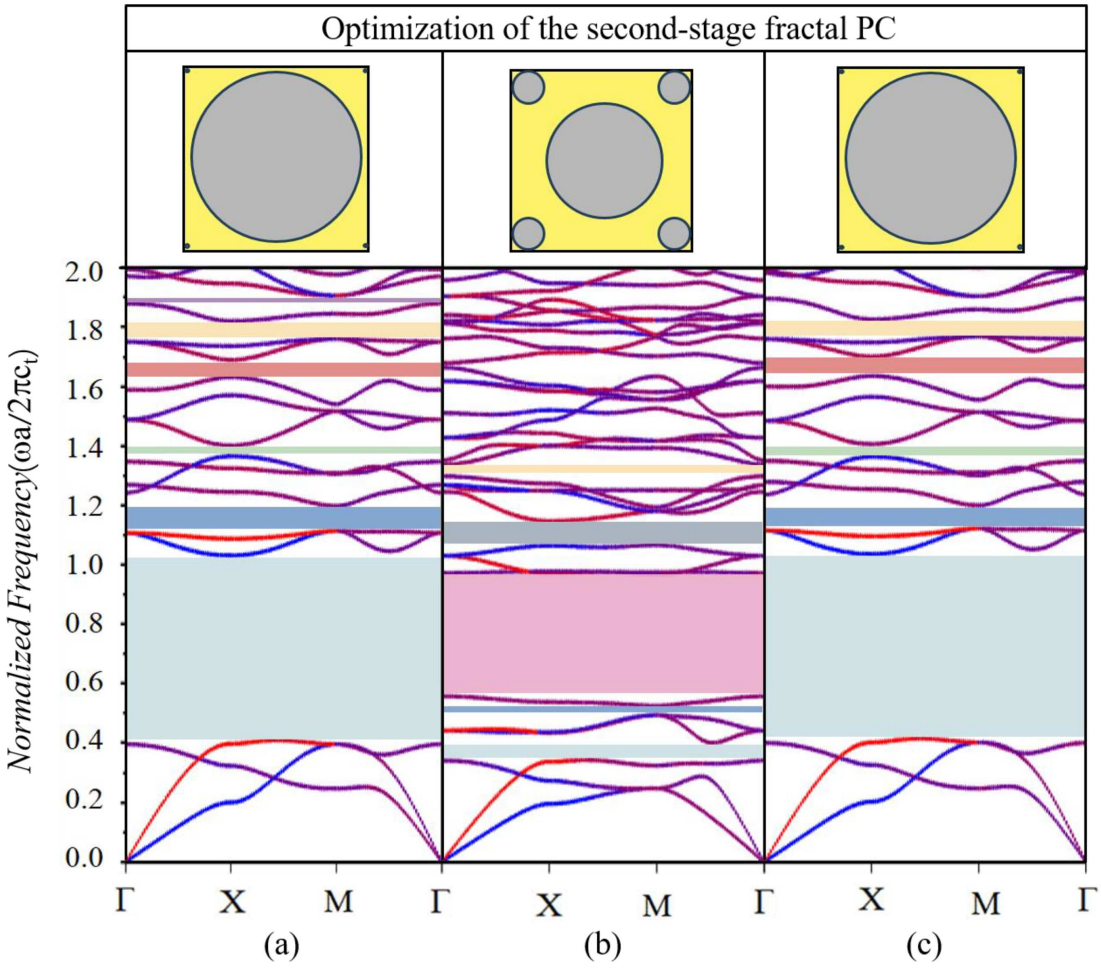

Figure 13. Optimized band structure of second-stage fractal PC using genetic algorithms: (a) widest 3rd–4th band gap, (b) widest 6th–7th band gap, (c) widest total band gap sum.

Figure 15b presents the band structure with structural parameters $r_1 = 0.3588\,a$, $r_2 = 0.0501\,a$, and $r_3 = 0.0083\,a$, resulting in the 6th–7th band gap width of 0.227. Lastly, Figure 15c shows the band structure with parameters $r_1 = 0.4328\,a$, $r_2 = 0.0118\,a$, and $r_3 = 0.009\,a$. Comparing these calculation results with those from Figure 13, it can be observed that the third-stage fractal PC is more conducive to opening mid to high-frequency band gaps than the second-stage fractal PC.

In conclusion, the optimization results of fractal PCs through genetic algorithms further validate the accuracy of the theories summarized in the previous section. Moreover, in terms of the second-stage structure, the third-stage structure is more effective in opening mid to high frequency band gaps within its band structure.

4 Conclusion

In this study, based on the concept of fractal PCs, we designed several fractal PCs with different filling ratios and measured and compared their band gaps. The results show that filling cores at different positions within the basic phononic crystal can influence the generation and widening of band gaps at various frequencies by altering the filling ratio of the cores. Filling cores in the central region of the basic phononic crystal primarily affects the formation of low-frequency band gaps; filling cores in the corner edges primarily affects mid-frequency band gaps; and filling cores at the center of the edges primarily affects high-frequency band gaps. Subsequently, this paper introduces a genetic algorithm for optimal design and discusses the widest band gaps between different bands and the overall widest band gaps in the band structures of second-stage fractal PCs and third-stage fractal PCs, verifying the accuracy of the proposed theory. Additionally, we found that compared to the second-stage structure, the third-stage structure is more effective in opening band gaps at mid to high frequency. This study provides a theoretical basis for the generation and regulation of band gaps at different frequencies in phononic crystals, particularly filling the current research gap regarding the generation methods and regulation of high-order band gaps in phononic crystals.

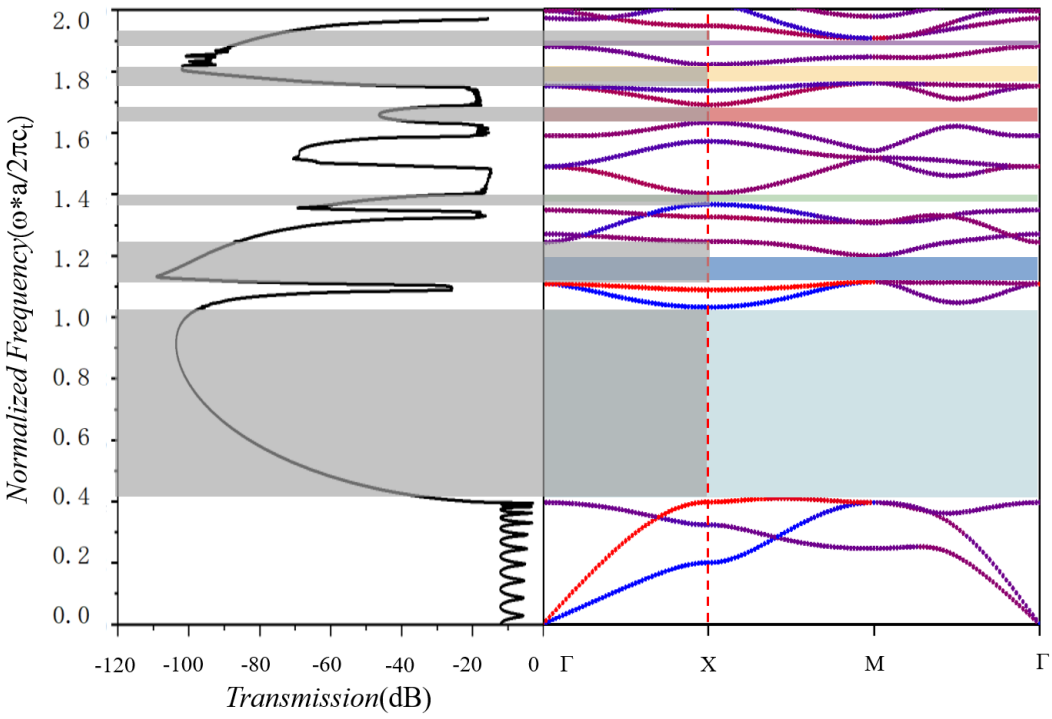

Figure 14. The band structure and response spectrum along the $\Gamma - X$ direction of the second-stage fractal structure when the 3rd–4th band gap is the widest.

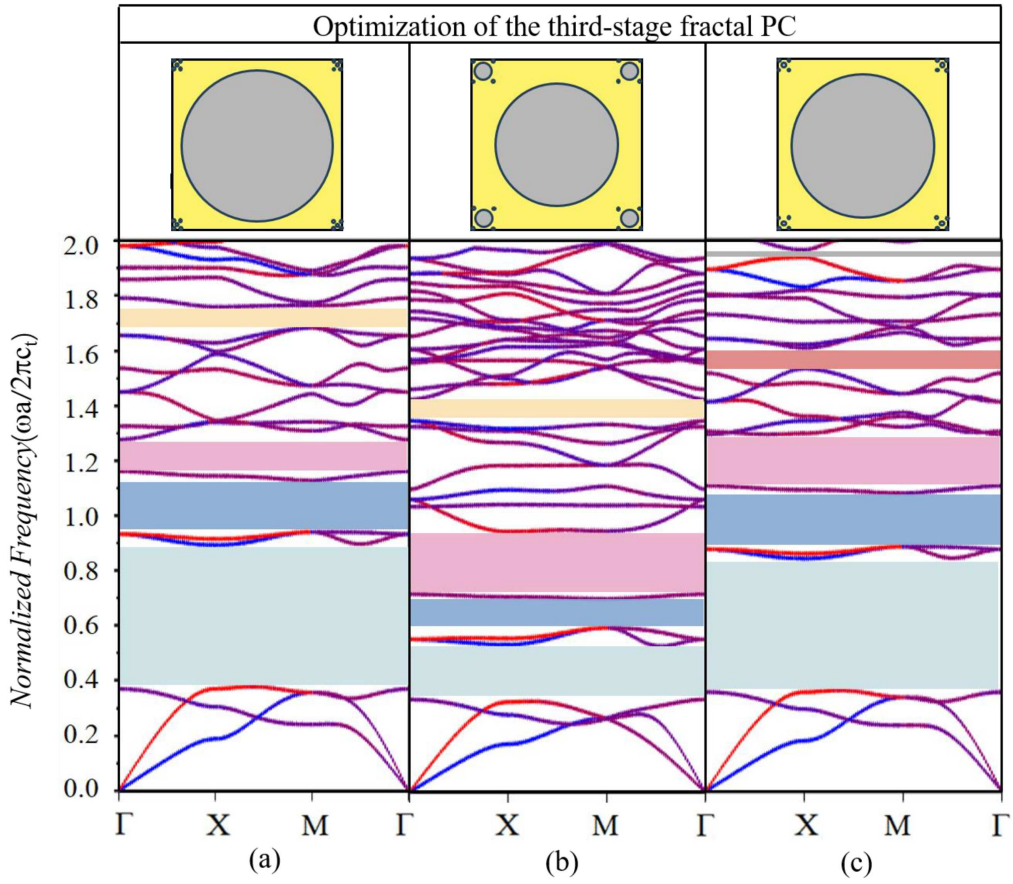

Figure 15. Optimized band structure of third-stage fractal PC using genetic algorithms: (a) widest 3rd–4th band gap, (b) widest 6th–7th band gap, (c) widest total band gap sum.

Funding

The authors acknowledge the support from National Natural Science Foundation of China (12302118), Higher Education Key Scientific Research Project of Henan Province of China (25B130001), Key Scientific and Technological Projects of Henan Province of China (242102320370) and Higher Education Teaching Reform Research and Practice Project of Henan Province of China (2024SJGLX0157).

Conflicts of interest

The authors declare that they have no known competing financial interests or personal relationships that could have appeared to influence the work reported in this paper.

Data availability statement

Data are available on request from the authors.

References

1. D. Tallarico, A. Bergamini, B. Van Damme: Long-range order Bragg scattering and its effect on the dynamic response of a Penrose-like phononic crystal plate. Physical Review B 107 (2023) 174201.
2. H. Xiang, Z. Chai, W. Kou, H. Zhong, J. Xiang: An investigation of the energy harvesting capabilities of a novel three-dimensional super-cell phononic crystal with a local resonance structure. Sensors 24 (2024) 361.
3. S. Yang, Y. Liu, T. Liang: Band structures in the nematic elastomers phononic crystals. Physica B: Condensed Matter 506 (2017) 55-64.
4. K.Y. Lee, W. Jeon: Hierarchical phononic crystals for filtering multiple target frequencies of ultrasound. Scientific Reports 10 (2020) 8070.
5. Z.-G. Chen, J. Zhao, J. Mei, Y. Wu: Acoustic frequency filter based on anisotropic topological phononic crystals. Scientific Reports 7 (2017) 15005.
6. S. Yang, X. Zhou, Y.-F. Wang: Tunable band gap and wave guiding in periodic grid structures with thermal sensitive materials. Composite Structures 290 (2022) 115536.
7. S. Yang, X.-L. Zhou, C.-Q. Li, S.-K. Zhang: Geometry optimization for tunable band gap and wave guiding in periodic grid structures. Modern Physics Letters B 35 (2021) 2150508.
8. S. Yang, L. Chang-Qing, L. Hong-Ju, W. Yan-Feng: Negative refraction and guided waves in fluid-solid phononic crystals. Journal of Harbin Engineering University 43 (2022) 1370–1375.
9. X.-L. Zhou, S. Yang, J.-R. Li, Z.-G. Bian, Y.-L. Shi: A tunable planar acoustic waveguide based on non-uniform period thermal fields. Modern Physics Letters B 37 (2023) 2350152.
10. N.F. Declercq: Rayleigh angle incident ultrasonic beam shape design influence on reflected beam. Acta Acustica 7 (2023) 41.
11. G. Yin, P. Li, X. Yang, Y. Tian, J. Han, W. Ren, J. Guo: Characteristics and mechanism of coupling effects in parallel-cladded acoustic waveguides. Acta Acustica 6 (2022) 8.
12. X.-L. Zhou, J.-H. Yin, K. Wang, S. Yang, L. Cao, P.-Y. Guo: Band gap tuning and wave separator design in 3d composite slab structures based on periodic thermal fields. Mechanics of Advanced Materials Structures (2024) 1–9.
13. Z. Bian, S. Yang, X. Zhou, D. Hui: Band gap manipulation of viscoelastic functionally graded phononic crystal. Nanotechnology Reviews 9 (2020) 515–523.
14. T.-X. Ma, Q.-S. Fan, C. Zhang, Y.-S. Wang: Flexural wave energy harvesting by the topological interface state of a phononic crystal beam. Extreme Mechanics Letters 50 (2022) 101578.
15. X.-L. Tang, T.-X. Ma, Y.-S. Wang: Topological rainbow trapping and acoustic energy amplification in two-dimensional gradient phononic crystals. Applied Physics Letters 122 (2023) 112201.
16. T.-X. Ma, Z.-Y. Li, C. Zhang, Y.-S. Wang: Energy harvesting of Rayleigh surface waves by a phononic crystal Luneburg lens. International Journal of Mechanical Sciences 227 (2022) 107435.
17. J. Xiao, X. Ding, W. Huang, Q. He, Y. Shao: Rotating machinery weak fault features enhancement via line-defect phononic crystal sensing. Mechanical Systems Signal Processing 220 (2024) 111657.
18. F. Ciampa, A. Mankar, A. Marini: Phononic crystal waveguide transducers for nonlinear elastic wave sensing. Scientific Reports 7 (2017) 14712.
19. Z.A. Zaky, M. Mohaseb, A.S. Hendy, A.H. Aly: Design of phononic crystal using open resonators as harmful gases sensor. Scientific Reports 13 (2023) 9346.
20. T. Zhu, T.-T. Wang, H.-T. Zhou, Y.-F. Wang, Y.-S. Wang: Reconfigurable phononic crystal sensor for liquid detection. Smart Materials and Structures 33 (2024) 035016.
21. J.O. Vasseur, P.A. Deymier, B. Chenni, B. Djafari-Rouhani, L. Dobrzynski, D. Prevost: Experimental and theoretical evidence for the existence of absolute acoustic band gaps in two-dimensional solid phononic crystals. Physical Review Letters 86 (2001) 3012.
22. Y. Pennec, B. Djafari-Rouhani: Fundamental properties of phononic crystal. Phononic Crystals (2016) 23–50.
23. S. Yang, Y. Liu: Effects of thermo-order-mechanical coupling on band structures in liquid crystal nematic elastomer porous phononic crystals. Ultrasonics 88 (2018) 193–206.
24. Y. Wang, X. Xu, L. Li: Advances in tunable bandgaps of piezoelectric phononic crystals. Materials 16 (2023) 6285.
25. S.V. Valappil, A.M. Aragón, H. Goosen: Phononic crystals' band gap manipulation via displacement modes. Solid State Communications 361 (2023) 115061.
26. N. Roth, A.L. Goodwin: Tuning electronic and phononic states with hidden order in disordered crystals. Nature Communications 14 (2023) 4328.
27. L.M. Weituschat, I. Castro, I. Colomar, C. Everly, P.A. Postigo, D. Ramos: Exploring regenerative coupling in phononic crystals for room temperature quantum optomechanics. Scientific Reports 14 (2024) 12330.
28. T.-Y. Fang, X.-W. Sun, X.-D. Wen, Y.-X. Li, X.-X. Liu, T. Song, Y.-Z. Song, Z.-J. Liu: High-performance phononic crystal sensing structure for acetone solution concentration sensing. Scientific Reports 13 (2023) 7057.
29. Y. Ruan, X. Liang: 2D phononic-crystal Luneburg lens for all-angle underwater sound localization. Acta Acustica 6 (2022) 12.
30. N.-K. Kuo, G. Piazza: Fractal phononic crystals in aluminum nitride: an approach to ultra high frequency bandgaps. Applied Physics Letters 99 (2011) 163501.

31. X.-J. Liu, Y.-H. Fan: Band structure characteristics of T-square fractal phononic crystals. Chinese Physics B 22 (2013) 036101.
32. K. Wang, Y. Liu, T. Liang: Band structures in Sierpinski triangle fractal porous phononic crystals. Physica B: Condensed Matter 498 (2016) 33–42.
33. J. Huang, Z. Shi, W. Huang: Multiple band gaps of phononic crystals with quasi-Sierpinski carpet unit cells. Physica B: Condensed Matter 516 (2017) 48–54.
34. Q. Wei, J. Xiang, W. Zhu, H. Hu: WBEM-based analysis of band structures of solid-solid and fluid-fluid phononic crystals with frequency-independent fundamental solutions. Engineering Analysis with Boundary Elements 151 (2023) 439–456.
35. Y.-J. Xin, P.-C. Cai, P. Li, Y. Qun, Y.-T. Sun, D. Qian, S.-L. Cheng, Q.-X. Zhao: Comprehensive analysis of band gap of phononic crystal structure and objective optimization based on genetic algorithm. Physica B: Condensed Matter 667 (2023) 415157.
36. X. Wen, L. Kang, X. Sun, T. Song, L. Qi, Y. Cao: Topological design of two-dimensional phononic crystals based on genetic algorithm. Materials 16 (2023) 5606.

Cite this article as: Yang S. Yin J.-H. Zhu X.-J. Wang K. Zhang S.-K. Cao L. Guo P.-Y. & Liu Y. 2025. Investigation and optimal design of band gap tunability in fractal phononic crystals. Acta Acustica, **9**, 18. https://doi.org/10.1051/aacus/2025007.